Predicting particle quality attributes of organic crystalline materials using Particle Informatics

Powder Technology 443 (2024) 119927

Contents lists available at ScienceDirect

Powder Technology

journal homepage: www.journals.elsevier.com/powder-technology

Predicting particle quality attributes of organic crystalline materials using Particle Informatics

Emilia Prandini [a], Eleonora Calì [a], Andrew G.P. Maloney [b], Emmanuele Parisi [a], Elena Simone [a,*]

[a] Department of Applied Science and Technology (DISAT), Politecnico di Torino, Torino, Italy
[b] The Cambridge Crystallographic Data Centre, 12 Union Road, Cambridge CB2 1EZ, United Kingdom

HIGHLIGHTS

- Particle Informatics tools were developed and tested for organic compounds.
- Crystal structure was linked to physical and chemical properties.
- Particle Informatics enable understanding of desolvation behaviour.
- Facet specific properties of a quercetin solvate were simulated.

GRAPHICAL ABSTRACT

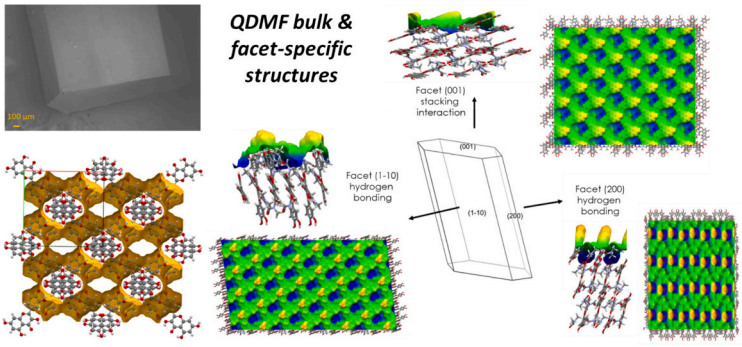

ARTICLE INFO

Keywords:
Particle informatics
Crystal engineering
Solvate
Quercetin
Modelling
Surface properties

ABSTRACT

In this work, a novel quercetin solvate of dimethylformamide (QDMF) was studied. The crystal structure was solved using single crystal X-ray diffraction and analysed using synthon analysis and other particle informatics tools (*e.g.*, solvate analyser). The thermal behaviour and thermodynamic stability of QDMF were studied experimentally using Raman spectroscopy, ATR-FTIR spectroscopy, differential scanning calorimetry, and thermogravimetric analysis. A clear relationship between the two-step desolvation behaviour of QDMF and the type, strength, and directionality of the main bulk synthons characterizing the QDMF structure was observed. Additionally, the attachment energy model was used to predict the QDMF morphology, together with facet-specific topology and chemical nature of each of the dominant {001}, {110}, and {200} facets. The {200} facet was found to be significantly rougher than the other two; whereas, the {110} was characterized by a higher percentage of exposed DMF molecules compared to the other two facets. Specific scanning electron microscopy and contact angle measurements were used to experimentally detect differences among the three facets and validate the modelling results.

* Corresponding author.
E-mail address: elena.simone@polito.it (E. Simone).

https://doi.org/10.1016/j.powtec.2024.119927
Received 8 April 2024; Received in revised form 24 May 2024; Accepted 25 May 2024
Available online 27 May 2024

1. Introduction

Organic crystalline particles are widely used in many applications, including the pharmaceutical, food and chemical industries. Crystal properties such as size, morphology, polymorphism, and surface features (*e.g.,* rugosity, facet-specific chemistry) can dramatically impact particle quality attributes such as solubility, flowability, rate of dissolution and stability at ambient conditions [1–3]. The design of crystallization processes that consistently deliver the desired crystal properties is challenging and is often supported by the use of process analytical technology (PAT) tools [4–6], different modelling techniques (*e.g.,* population balance, computational fluid dynamics) [7–10] and, more recently, data-driven approaches [11]. However, even more challenging is the determination of the exact crystal properties that affect specific quality attributes. Indeed, this task requires numerous and lengthy screening experiments during the product development stage to test the performance of crystalline particles with different size and shape distributions, or different polymorphic forms. Getting a clear understanding of the relationship between crystal structure and particle quality attributes is essential to reduce product development times, therefore it is the main goal of the so-called "crystal engineering" approach [1,2,12]. This approach has become very popular in the last decade and focused mainly on relating specific features of a crystal structure with specific particle properties such as stability [13], solubility, bioavailability [14,15] and, more recently mechanical strength [16,17]. Crystal structure visualization and modelling (*e.g.,* synthon analysis) are two powerful tools of crystal engineers and have been successfully used to explain relative thermodynamic stability of different solid forms of the same compound [18–22] and improved solubility and dissolution rate of co-crystal formulation [23]. More recently, researchers attempted to apply the same tools to relate crystal structure with more specific particle properties such as flowability [24,25] and facet-specific surface chemistry [21,26,27]. The result of these preliminary studies is the creation of the concept of "Particle Informatics", which has been introduced to describe a "workflow of digital design tools to better understand several stages in the formulation and manufacturing pipeline of small molecule pharmaceuticals" [17]. Each step of a characteristic Particle Informatics workflow provides a comprehensive understanding of particle behaviour and the analysis covers intermolecular interactions, prediction and evaluation of mechanical properties, calculation and examination of particle morphology, analysis of surface energy, and evaluation of surface interactions [28,29]. Nevertheless, we are still far from a robust methodology that can be universally applied for a complete digital design of crystal structures that target specific particle quality attributes. This is due to the difficulty in: (1) precisely measuring some specific particle properties such as flowability, wettability or facet-specific rugosity; (2) predicting the surface features of complex organic structures, such as solvates [30], salts, and co-crystals. In this work we attempt to address both these issues using computational tools (bulk synthon analysis [31], facet-specific topological analysis, and attachment energy models [32]) and experimental validation (X-ray indexing, scanning electron microscopy, facet-specific contact angle and Raman microscopy) for a complex organic structure, a quercetin solvate with *N*,*N*-dimethylformamide (QDMF).

Quercetin, also known as 2-(3,4-Dihydroxyphenyl)-3,5,7-trihydroxy-4H-chromen-4-one, is a naturally occurring flavonoid, a type of polyphenolic compound, present in numerous fruits and vegetables, such as onions, tomatoes, apples, and berries [33]. Flavonoids are natural compounds found throughout various plant species and parts of plants; due to their well-documented health-promoting properties they are widely studied for several food and biological applications [34]. Quercetin has gained substantial attention in recent years, emerging as one of the most extensively researched flavonoids [35]. This increasing interest is due to its numerous health benefits, including its role as an antioxidant, anti-inflammatory agent, and its potential antitumor properties [36]. However, it is widely reported that this compound shows poor bioavailability and low aqueous solubility ($\leq$ 20 μg/ml) [33,36] and so it has been classified as a class IV molecule in the Biopharmaceutical Classification System (BCS) [37]. For this reason, improving its dissolution and bioavailability is necessary to fully exploit its potential benefits. Quercetin has a peculiar molecular structure, with the co-existence of several OH groups that can form hydrogen bonds, and aromatic rings that can contribute to strong non-polar stacking interactions, such as $\pi - \pi$ interactions. The possibility to form both polar and non-polar interactions can determine crystal anisotropy, and improves the chances to form multicomponent crystal structures where quercetin molecules are bonded with water, solvents, or co-crystal co-formers [37–39]. Hence, quercetin is an excellent candidate for the validation of Particle Informatics tools, as its physical and chemical properties (*e.g.*, solubility, surface chemistry, bioavailability) can be tailored *via* the formation of different crystal structures.

2. Materials and methods

2.1. Materials

Quercetin dihydrate (QDH) with a purity of 97% was obtained from Thermo Fisher Scientific (Kandel, Germany), and used without purification or recrystallization; *N*, *N*-dimethylformamide (DMF) solvent was purchased from Sigma Aldrich (Steinheim, Germany).

2.2. Preparation of Quercetin in dimethylformamide (QDMF)

The quercetin dimethylformamide solvate (QDMF) was prepared by adding 300 mg of QDH in 470 mg of DMF; the solution was heated up from 20 °C to 80 °C to dissolve the powder and then was cooled down again to room temperature using the multi-reactor crystallizer Crystal16® V2 (Technobis Crystallization Systems, Alkmaar, The Netherlands). The solution was stirred using an overhead stirrer at 780 rpm, and heating and cooling rates of ± 0.5 °C min^{-1}. After nucleation in the Crystal16 the vials were kept open at ambient conditions for at least 5 days, to allow evaporation of the solvent and growth of the crystals.

2.3. Single Crystal X-ray diffraction (SCXRD)

To determine the crystal structure of the single crystals of suitable size, X-ray diffraction was performed with a Bruker-Nonius diffractometer equipped with a Kappa CCD detector (Delft, The Netherlands) and connected to an Oxford Cryostream 700 low-temperature device using mirror graphite monochromated Mo Kα radiation ($\lambda = 0.71073$ Å). Data reduction and semiempirical absorption correction were done using the SADABS [40] program. The structures were solved by direct methods (SIR97 program) [41] and refined by the full-matrix least-squares method on F^2 using SHELXL-2016 [42] with the aid of WinGX [43]. All carbon-bound hydrogen atoms were generated stereochemically and refined by the "riding model". After having placed C-bound H atoms, those bonded to N and O were clearly found in difference Fourier maps as the first maxima, and their coordinates were refined. For all H atoms, $U_{iso} = 1.2 \times U_{eq}$ of the carrier atom was assumed. The analysis of the crystal packing was performed using the program Mercury (CSD 2023.3.1) [44]. The face indexing of the crystal sample was carried out using CrysalisPro (v.171.42.49, Rigaku Oxford Diffraction) software and is reported in the SI (Fig. S1).

2.4. X-ray diffraction (PXRD, VT-PXRD)

The XRD patterns of powder samples were obtained on a Panalytical X'Pert Pro, which was set up in Bragg-Brentano configuration, using a Cu Kα radiation. The sample was scanned between 3° and 40° in 2θ with a step size of 0.01313° (2θ) and time per step of 29 s. The X-ray generator was set at a tube voltage of 40 kV and a current of 40 mA. Samples were prepared with a Si zero background and measured

without spinning. Furthermore, to observe the changes in XRD patterns on the Panalytical X'Pert Pro the temperature of samples was increased in steps from 25 to 150 °C at a rate of 10 °C min^{-1}.

2.5. Differential scanning calorimetry (DSC) and thermogravimetric analysis (TGA)

The thermal properties of QDMF were observed using a Mettler Toledo 8000 DSC-1 calorimeter (PerkinElmer). The differential scanning calorimeter was calibrated using indium. Initially, 6 mg of sample was accurately weighed into an aluminium pan. The lid was crimped in place and the sample heated from 25 to 350 °C at a heating rate of 10 °C min^{-1}. Nitrogen was used as the purge gas at 50 ml min^{-1}. The heat flow was measured in mW and through peak height, the melting point of the sample was determined. A Mettler Toledo TGA (1600, Columbus, OH, USA) was used for the thermogravimetric analysis. The sample was heated with a constant heating ramp of 10 °C min^{-1} from 25 °C to 350 °C while argon (Ar) was supplied at a constant flow rate (50 ml min^{-1}). To investigate the desolvation process during the two endothermic events, the TRIOS software was used for the enthalpy calculation $\Delta H_{S,exp}$ (J g^{-1}). The different onset temperatures of the desolvation processes indicate a different binding strength of the two molecules of solvent in the crystal. The solvent was lost in two steps and the percentage weight loss of solvate (Δm_S) was related to the enthalpy change calculated over the corresponding DSC desolvation endotherm ($\Delta H_{S,exp}$, in J g^{-1}) as in Eq. (1) [45]:

$$\Delta H_S = \left[\frac{\Delta H_{S,exp} \times 100}{\Delta m_S}\right] \times Ms \quad (1)$$

where ΔH_S (in J mol^{-1}) is the heat of vaporization of the QDMF and M_S the molecular weight of the solvent.

2.6. Raman spectroscopy

Raman spectra were acquired using a 785 nm laser source with a LabRAM HR Evolution spectrometer (HORIBA Scientific, France) equipped with a 10× and 100× objective. Backscattered radiation was collected with a Synapse Plus BIDD Detector (1024 × 256 pixels), utilizing a 300/nm grating. No filter was applied and the laser power was set at 100%. Spectra were acquired with a 1-s acquisition time for 35 accumulations. The first analysis was conducted at room temperature within the frequency range from 1690 to 1000 cm^{-1}. Principal Component Analysis (PCA) was performed on the set of accumulated spectra using the default *pca* function (data were smoothed with the *sgolay* default function) in MATLAB R2021a. The intensity of the first principal component score was projected on the x,y plane to generate the PCA maps. The x and y coordinates of the map ranged from −40 to 40 μm and from −30 to 30 μm, respectively. Temperature ramp measurements were performed with a LinkamPE120 hot stage connected to a water circulation pump (Linkam Scientific Instruments, UK). The temperature was then varied with a T96 Peltier LinkPad controller. Each sample was heated up to 110 °C at 10 °C min^{-1}. The Raman spectra were acquired every 10 °C with 1-s acquisition time for 10 accumulations.

2.7. Attenuated total reflection Fourier transform infrared spectroscopy (ATR-FTIR)

Spectra were collected on a Bruker Tensor 27 FT-IR spectrometer. Samples were measured from 400 to 4000 cm^{-1} at a resolution of 4 cm^{-1} and accumulating 64 scans. The data were processed using the Opus 8.2.28 software.

2.8. Scanning electron microscopy (SEM)

The morphology of the QDMF samples was investigated using a field-emission scanning electron microscopy (FE-SEM) Zeiss Merlin operating at a 3 kV voltage and a 100 pA probe current, equipped with an annular In-Lens secondary electron detector. SEM specimen preparation was carried out by placing single crystals on stubs with carbon tape both without further preparation or after cleavage (using a sharp razor blade after X-ray indexing) along the main crystallographic planes, particularly the (1−10) and the (001). Stubs and crystals were then coated with platinum for 30 s.

2.9. Contact angle measurement

Sessile drop measurements were conducted at room temperature using a DSA25 Drop Shape Analyzer (Krüss Scientific) equipped with a micro-syringe and a high-speed camera. Single crystals of QDMF of suitable size (few mm length and width) were placed in the measuring chamber, lying flat on their largest facets (the {110} and {200}). Water droplets (0.5 μl) were dispensed onto the horizontal facet using a straight needle, and the droplet behaviour was recorded with a camera. The droplet contour was analysed using the Young-Laplace method, and the contact angles between the particle substrate and the water droplet were determined. Each measurement was performed three times to ensure accuracy.

2.10. Computational procedures

The Materials Studio 2021(v21.1.1.3268) and Mercury (CSD 2023.3.1) programs were used for the computational analysis; the latter software was also used for the visualization of the bulk and facet structures. Fig. 1 shows the workflow used for the computational modelling.

The structure minimization and the optimization of unit cell parameters were performed using the Forcite module in Materials Studio 2021. The torsion angle between the phenyl and pyrone moieties was kept rigid. The SMART algorithm was selected for the structural minimization with the Dreiding forcefield [26]. General force constants and geometry parameters for this forcefield are based on simple hybridization rules rather than on specific combinations of atoms. The van der Waals interactions are described by the Lennard-Jones potential. Electrostatic interactions are described by atomic monopoles and a screened (distance-dependent) Coulombic term. Hydrogen bonding is described by an explicit Lennard-Jones 12–10 potential. The optimization parameters are reported in Table S3.

The intrinsic synthon analysis and calculation of the intermolecular interactions analysis were carried out with the Visual Habit module in the CSD-Particle suite in Mercury, between a fixed molecule and all the other molecules within a limiting radius of 30 Å. The Dreiding II [46] forcefield was used for this calculation.

Before analysing the surface topology, the experimental morphology obtained *via* X-ray indexing was imported in Mercury to simulate only the facets that are present in the observed QDMF crystals. The cell parameters, the facet miller indices and the hkl distances were input as a .cif file in Mercury to build the experimental crystal morphology and calculate the relative areas of the different facets. The attachment energy model was applied to calculate the specific synthons contributing to the growth of the experimental facets and to simulate their topology (*e.g.,* rugosity [47,48], densities of H-bond donors, H-bond acceptors, aromatic bonds). This was also carried out with the calculated Visual Habit morphology through the Surface Analysis tool in CSD-Particle. A script using the CSD Python API (a link to the script is provided in the SI) was used to further analyse the chemical nature of each facet obtained with the attachment energy model. Briefly, this script uses the individual surface nodes that make up each topological surface and identifies the percentage surface area attributable to each individual atom type. Due to minor overlap of these surface nodes for each atom type, the total percentage calculated for all atoms does not equal 100%.

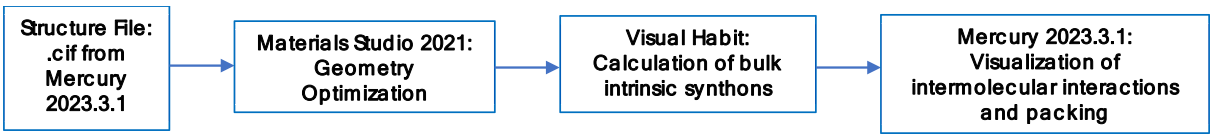

Fig. 1. Workflow used in this work for computational modelling.

3. Results & discussion

3.1. Crystal structure characterization

The crystallization of the QDMF solvate was carried out by cooling experiments, followed by slow evaporation of the solvent in a stable place until the precipitation of crystals with adequate size for single-crystal X-ray analysis (Fig. 2A).

The QDMF structure was solved from single-crystal diffraction data collected at 173 K and the relevant crystallographic parameters are shown in Table 2. Further details of the data collection and structure refinement are provided in Table S1. The structure is monoclinic (*C*2/c) with one quercetin molecule and two DMF molecules in the asymmetric unit (Fig. 2C).

In the structure of quercetin, the pyrone and phenyl rings are not coplanar; instead, they form a dihedral angle τ of 15.68(2)° between the average planes. Comparing the dihedral angle values with those of other known quercetin solvate structures (Quercetin monohydrate (QMH), Quercetin dihydrate (QDH), and Quercetin in dimethyl sulfoxide (QDMSO)), the torsion angle value becomes smaller (Table 1) when the quercetin molecules are stacked with a more compact geometry, involving either hydrogen bonds or stacking interactions (hydrogen bonds are reported in Table S2).

The crystal packing of QDMF is shown in Fig. 3. Molecules are arranged in undulated ribbons formed by strong H-bonding between hydroxyl donor and carbonyl acceptor groups (1.928(2) Å and 2.103(2) Å distances) with the formation of R_2^2 (10) ring motifs. Each quercetin molecule is involved in two strong hydrogen bonds with the two DMF solvate molecules (distances of 1.778(2) Å and 1.788(2) Å).

Fig. 4A was obtained using the Voids calculation tools integrated within the Mercury software. It highlights, in yellow, the volume occupied by the DMF molecules in the crystal packing of the QDMF structure, representing 23.9% of the unit cell volume. From Fig. 4B, it is possible to highlight how the two DMF molecules are differently arranged inside the crystal packing. In particular, the DMF molecules, red and blue, occupy 7.2% and 5.2% of the total surface structure, forming channels and pockets respectively. This structural feature could be associated with the time-step desolvation process observed during the thermal analysis.

3.2. Thermodynamic stability of QDMF

The DSC curve for QDMF exhibited three main endothermic events, as shown in Fig. 5. The first and the second one can be associated with desolvation processes, as shown by thermogravimetric analysis reported in the same figure. Desolvation occurs at high temperatures (approximately 103 °C and 171 °C, respectively), which suggests that the solvent molecules are strongly bound in the crystal structure [49]. These values of onset temperature are similar to those reported for desolvation of other quercetin solid forms, such as the dihydrate (95 °C) and the quercetin DMSO solvate (136 °C) [35,50]. The third sharp endothermic peak is related to the melting point of quercetin and occurred at approximately 314 °C, which agrees with the corresponding value

Table 1
Torsion angle values between pyrone and phenyl rings of quercetin solvate and hydrates forms.

	QA	QMH	QDH	QDMSO	QDMF
CSD Refcode	NAFZEC02	AKIJEK	FEFBEX02	VUVHOM	N/A
Torsion Angle °	20.73(3)	−1.04 (3)	6.50(3)	30.71(3)/ 31.11(3)	15.63 (3)

Table 2
Crystallographic information for QDMF.

Temperature/K	173.15
Formula	C_{15} H_{10} O_7,2(C_3 H_7 N O)
Z,Z′	8,1
crystal system, space group	monoclinic, C2/c
a/Å	20.840(5)
b/Å	17.109(4)
c/Å	13.736(3)
α/°	90
β/°	119.42(2)
γ/°	90
cell volume/Å^3	4266.01
cell density/g cm^{-3}	1.396
μ/mm^{-1}	0.110

Table 3
Thermogravimetric and calorimetric data for QDMF solvate.

Endothermic peaks	Desolvation onset temperature (°C)	Desolvation enthalpy change $\Delta H_{S,exp}$ (J g^{-1})	Percent mass loss Δm_S%	ΔH_S (kJ mol^{-1})
1	95	66.57	10.5	46.3
2	146	92.36	22	30.6

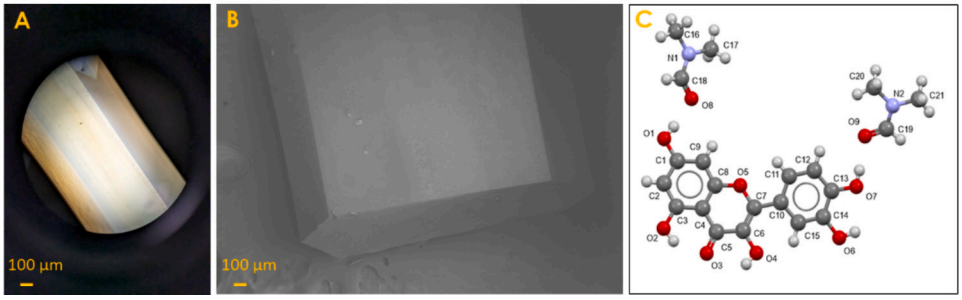

Fig. 2. Micrograph (A), SEM image (B), and chemical structure of QDMF crystals (C).

Table 4
Summary of intermolecular interactions in QDMF structure.

interaction number	molecules	interaction type	centroid-centroid distance (Å)	interaction energy (kcal mol^{-1})	% to total lattice energy
interaction 1	quercetin - quercetin	hydrogen bond	11.29	−6.15	19.4%
interaction 2	quercetin - quercetin	off-set stacking	5.04	−5.99	18.9%
interaction 3	quercetin - quercetin	off-set stacking	4.64	−5.36	16.9%
interaction 4	quercetin – DMF1	hydrogen bond	8.67	−3.33	10.5%
interaction 5	quercetin - DMF2	hydrogen bond	9.40	−3.24	10.2%
				Total	75.9%

Table 5
Indexed morphology analysis performed by importing SCXRD data in Mercury.

Form	Multiplicity	Facets	Relative area (%)	Total form area (%)
{001}	2	(001)	11	22
		(00−1)	11	
{110}	4	(110)	10	55
		(1–10)	18	
		(−110)	17	
		(−1−10)	9	
{200}	2	(200)	11	23
		(−200)	12	

Table 6
Parameters calculated through the surface analysis to determine the rugosity of forms and identify the predominant exposure of H-bond donor, H-bond acceptor, or aromatic groups, which largely compose the terminations of main facets. The rugosity is calculated as the ratio between the total area of the specific facet and the projected area of the same portion of the facet.

Form	Multiplicity	Rugosity	Donors (count/ Å^2)	Acceptors (count/ Å^2)	Aromatics (count/ Å^2)
{001}	2	1.353	0.047	0.063	0.094
{110}	4	1.604	0.017	0.044	0.000
{200}	2	2.230	0.036	0.067	0.079

Table 7
Surface chemistry coverage for different facets estimated with the CSD Python API.

Atom Type	Molecule	(001) Percentage Coverage	(1–10) Percentage Coverage	(200) Percentage Coverage
aromatic C	Quercetin	35.419	–	30.828
sp^3 O	Quercetin	31.895	5.156	21.617
amide N	DMF	1.251	4.619	1.430
sp^3 C	DMF	4.452	26.926	12.817
sp^2 C	quercetin, DMF	9.934	13.445	13.582
sp^2 O	quercetin, DMF	7.685	16.886	8.536
H	quercetin, DMF	41.222	62.066	46.559

reported in literature. The melting is followed by an exothermal peak at 356 °C attributable to chemical decomposition.

Combining the TGA analysis in Fig. 5, the curve obtained for QDMF exhibited a three-step weight loss. Considering complete desolvation of QDMF, the total theoretical weight loss (stoichiometry 1:2, quercetin to dimethylformamide) should be 32.6%. The observed loss from TGA is

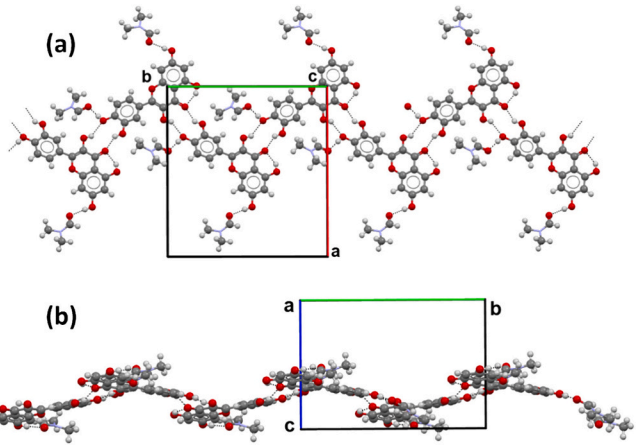

Fig. 3. Packing view of QDMF: a) view along the *c* axis showing the hydrogen bonds (light grey) between quercetin-quercetin and quercetin-DMF molecules; b) view along the *a* axis.

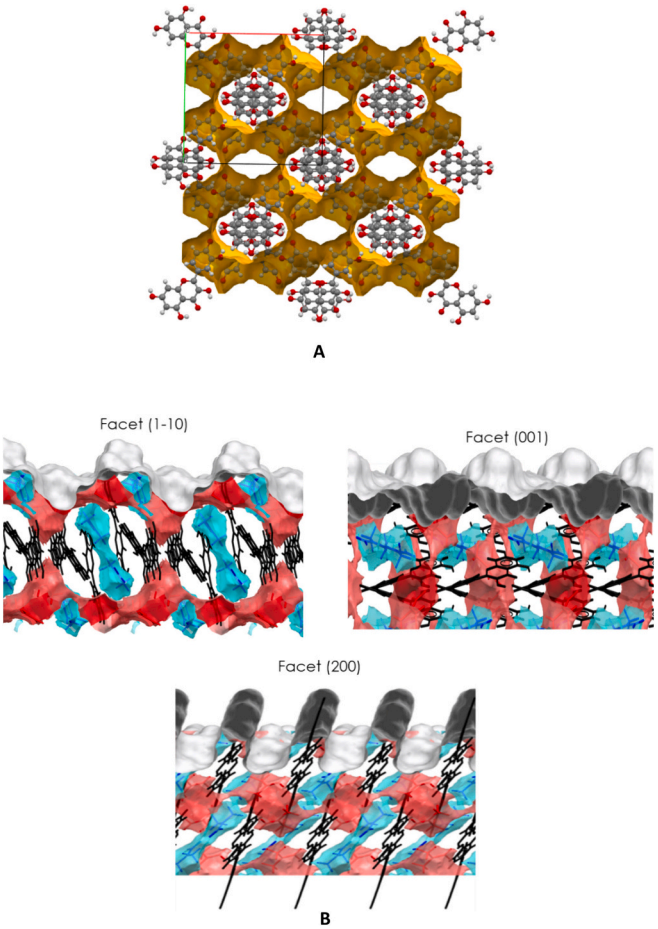

Fig. 4. Void calculation representation (A) and Solvate Analyser images for the three different facets (B).

around 32%, which is consistent with the theoretical value. The first loss in mass is 10%, with an onset temperature of 95 °C and finishing at 112 °C. A second weight loss event occurs between 146 °C and 177 °C, with a higher mass loss of 22%. These thermal events, also observed previously in the DSC curves, should correspond to the complete loss of the solvent incorporated into the crystal.

The theoretical enthalpy of desolvation was calculated with TRIOS

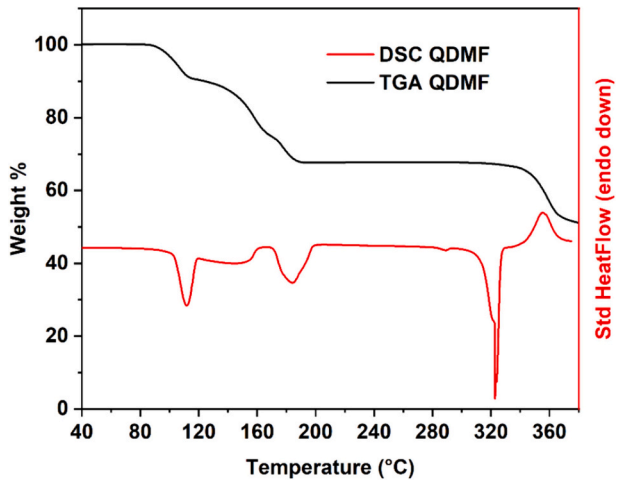

Fig. 5. DSC (red) and TGA (black) curves obtained on QDMF. (For interpretation of the references to colour in this figure legend, the reader is referred to the web version of this article.)

and the results are shown in Table 3. When comparing the ΔH_S values, it is evident that the first desolvation step takes slightly more energy than the second one.

To investigate the structural changes in QDMF when the temperature is increased, variable temperature PXRD analysis was performed. Results are illustrated in Fig. 6; the main diffraction peak of QDMF from 25 to 75 °C is at 7.0°, and it decreases in intensity when the temperature reaches 100 °C. Other changes are evident in the XRD patterns, indicating structural changes that are related to the desolvation phenomena observed in the DSC and TGA. It is worth noting that, despite the presence of channels in the QDMF crystal lattice, the desolvation process does not preserve the structure, perhaps due to the strong interactions between quercetin and DMF molecules (as shown in the following sections). The desolvation process leads to the formation of an anhydrous form of quercetin, with a diffraction pattern-similar to that of the desolvated crystalline forms reported by Klitou et al. [35] (Fig. S2).

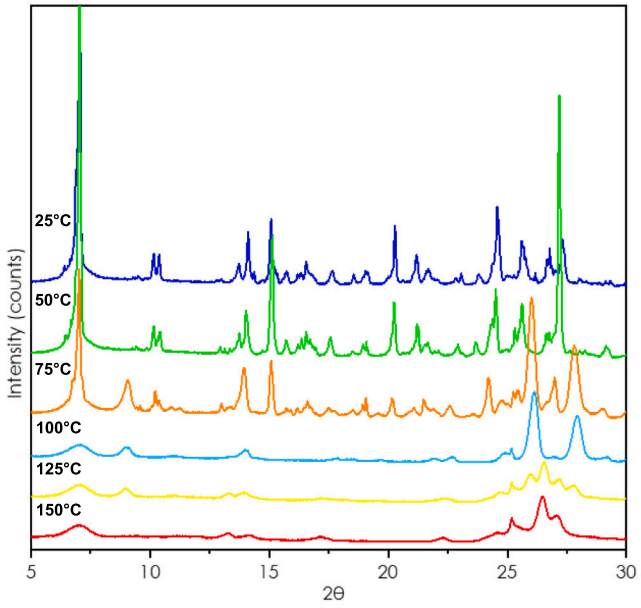

Fig. 6. Variable temperature-powder X-ray diffraction patterns of QDMF.

3.3. Bulk intermolecular interactions of QDMF

The five strongest intermolecular interactions in the QDMF structure are summarized in Fig. 7. For every interaction, the view in the lattice along a specific axis is reported, together with a view of the two molecules that are responsible for the interaction. Table 4 illustrates the distance, the interaction energy, and the contribution to the total lattice energy for each synthon. The strongest interaction, interaction 1, is a hydrogen bond between two quercetin molecules, located along the *b* axis of the unit cell. The nonplanar conformation of the quercetin molecules facilitates close contact between the acceptor and donor groups.

The second and third strongest interactions, interaction 2 and interaction 3, are parallel displaced off-set stacking interactions between two quercetin molecules with longer stacking distances (4.64 Å and 5.04 Å) than the quercetin dihydrate form (3.67 Å) but comparable with other solvates/hydrates quercetin crystalline forms (4.85 Å Quercetin monohydrate, 5.05 Å Quercetin-DMSO) [50], suggesting a less dense packing of the molecules in the crystal structure. The primary factor influencing this form of interaction arises from the aromatic carbon atoms found in the phenyl and pyrone rings of quercetin molecules. These interactions occur through attractive Van der Waals forces, and they facilitate the creation of continuous chains of quercetin molecules arranged in a staggered orientation. Each quercetin interacts with two different DMF molecules through two different hydroxyl groups of the quercetin molecule.

The interaction energies of the two synthons are very similar, with similar interaction geometries between the two synthons. However, only one of the two DMF molecules (DMF1 in Fig. 8) has its centroid in the average molecular plane of quercetin (interaction 4), while the other (DMF2 in Fig. 8) is slightly displaced by 1.823 Å.

This geometric difference can affect the desolvation process of the crystal structure, which starts with the expulsion of the DMF molecule involved in the interaction 5 synthon, and a subsequent co-expulsion with the other DMF molecule involved in the interaction 4 synthon, that is in line with a time-step desolvation event as shown from the thermogravimetric analysis reported in Fig. 5.

These five interactions contribute to over 75% of the total lattice energy; it is evident that the total lattice energy is dominated by hydrogen bond interactions, allowing the formation of infinite ribbon chains along the *b* axis, while the contribution of the off-set stacking helps the undulated layers to interact more closely.

ATR-FTIR spectroscopy was further performed to elucidate the hydrogen bond interactions between the solvent and quercetin molecules (Fig. S3). We have compared the QDMF spectrum with that of quercetin dihydrate (QDH), whose structure is well known. Both spectra show multiple dense clusters of overlapping peaks in the region between 1700 and 400 cm^{-1}. The functional groups involved in hydrogen bonding (hydroxyl and carboxylic groups) are the same in both the compounds, but the stretching mode of –C=O (1660 (QDH) and 1641 (QDMF) cm^{-1}) and the bending mode of –OH (1380 (QDH) and 1312 (QDMF) cm^{-1}) in the QDMF spectrum are shifted at lower frequency (red shift) compared to QDH. This indicates a closer distance of the hydrogen bonding interaction. Moreover, the QDMF compound shows a strong sharp peak related to the –OH stretching at 3351 cm^{-1}, which is instead broad and weak in the QDH spectrum due to the presence of water molecules in the structure.

The prevalence of hydrogen bonding in the structure of QDMF is likely the reason for its hydrophilic nature, as shown by the water contact angle measured on single crystals (Fig. S4), which was measured as 33.7 ± 10.8° (mean value of the {200} and {110} facets). It was noted that water droplets were quickly adsorbed by the single crystals during the measurements, possibly due to the high affinity of the QDMF for water.

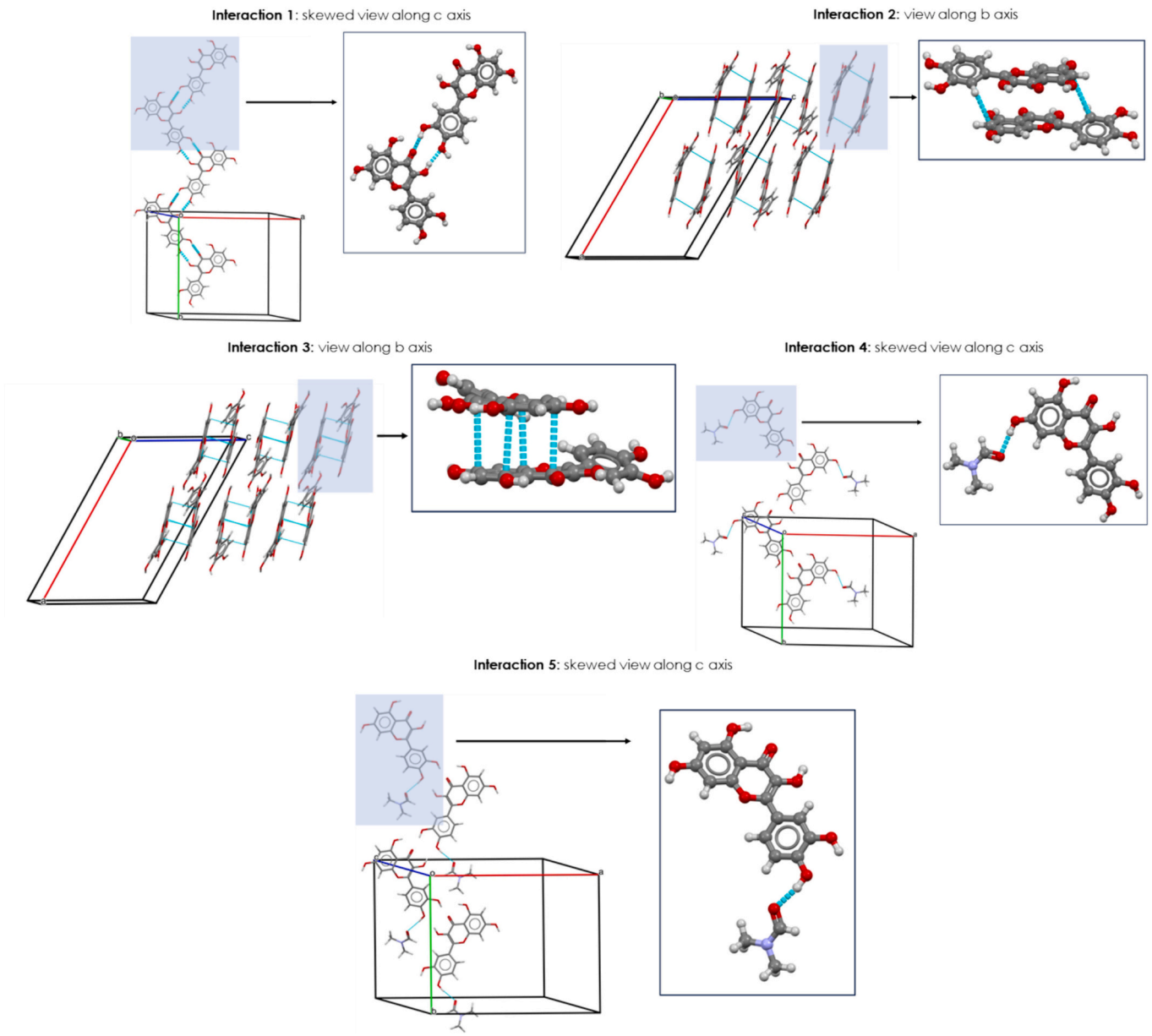

Fig. 7. Principal intermolecular interactions (light blue) in QDMF that contribute most to the total lattice energy, ordered by strength. (For interpretation of the references to colour in this figure legend, the reader is referred to the web version of this article.)

3.4. Crystal surface experimental and simulated features

The morphology analysis performed with Mercury on the experimentally indexed crystals (Table 5) revealed the presence of three prevalent facets in the obtained QDMF crystals: the {110}, accounting for 55% of the total crystal surface, the {001}, and the {200}, measuring 22 % and 23%, respectively. The simulated morphology obtained from the attachment energy model is reported in (Fig. S5).

Through application of the attachment energy model, it was found that the dominant interaction contributing to the growth of the (001) facet is the stacking interaction between quercetin molecules, as shown in Fig. 9. For the other two main facets exposed, (1–10) and (200), the primary contributing interaction is the hydrogen bonding between quercetin molecules. Analysing the surface, the contribution of aromatic bonds, H-bond donors, and H-bond acceptors is more evident on the (001) facet, due to the prevalence of quercetin molecules on this surface since these molecules terminate with aromatic carbons, OH donor groups, and O-atoms of carbonyl and hydroxyl groups, which can act as acceptors. Conversely, the (1–10) and (200) facets exhibit fewer of these functional groups. There is no presence of aromatic bonds on the (1–10) facet and the presence of acceptors and donors is considerably lower, as illustrated in Table 6. The lower incidence of aromatic groups present on these surfaces is in line with the water contact angle values measured, which indicate the hydrophilic nature of the two largest facets.

Table 6 also shows another parameter that can be calculated from crystallographic data, *e.g.,* the facet-specific atomic rugosity (visually represented in Fig. 9). While the (200) facet has higher rugosity compared to the other two facets, none of the surfaces can be considered "smooth".

To experimentally assess the calculated facet-specific rugosity, SEM was carried out on cleaved crystals. Non-cleaved crystals were also analysed, but the presence of secondary nucleation particles and desolvation effects (Fig. S6), did not allow a full overview of the nanoscopic surface features. Hence, cleavage was performed to expose fresh facets and identify clearly the desired crystallographic planes to analyse. Fig. 10 shows the (001) and (1–10) facets exposed after cleavage at

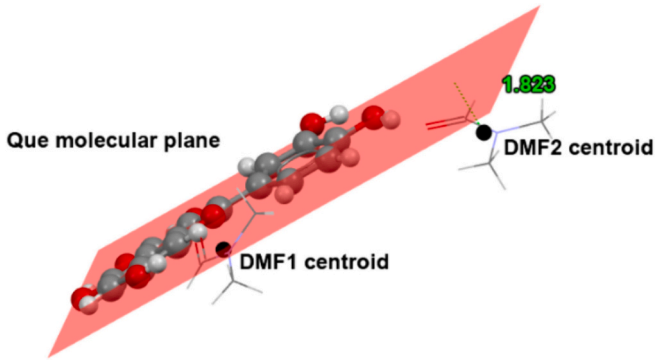

Fig. 8. Molecular displacement of DMF molecules. In red the molecular plane of the quercetin calculated by considering all the molecular backbone atoms. In black the molecular centroids of the two different DMF molecules calculated by considering all the atoms of the molecular backbone. (For interpretation of the references to colour in this figure legend, the reader is referred to the web version of this article.)

different magnifications. The scale of the surface features observed in the SEM is much larger than that observed in the simulated topologies (Fig. 9); nevertheless, regular nano-sized surface patterns are still evident for both facets and similar to the simulated morphologies. The rugosity of the two analysed facets is similar, in accordance with the calculated results shown in Table 6. Facet (001) presents a slightly higher rugosity compared to the other facets, due to the presence of a higher concentration of higher hills and deeper valleys on its surface. The surface features characterizing facet (1–10) are less deep, and more rounded compared to those of facet (001). This is in disagreement with the modelling results, which showed slightly higher rugosity for facet (1–10). However, it is possible that cleavage induced plastic deformation of the exposed (1–10) facets, reducing its rugosity (which might explain the more rounded features for this facet). Plastic deformation was noticed in other cleaved crystals, which were cut less carefully that that of Fig. 10, as shown in Fig. S7. This facet specific tendency to plastic deformation might be due to the different nature of the intermolecular interactions that contribute to these facets: strong hydrogen bonds for the (1–10) and off-set stacking for the (001).

The CSD Python API was used to assess the percentage coverage of the different atoms of quercetin and DMF molecules on the different facets. This method confirmed that the (001) facet exhibits greater exposure of the quercetin molecules: Table 7 demonstrates that the presence of aromatic carbon and sp^3 oxygen, both of which are characteristic of quercetin molecules, on this facet is considerably higher compared to the other facets. The (1–10) facet instead has a higher percentage of DMF molecules, characterized by the presence of nitrogen and sp^3 carbon atoms.

This helps to explain why the desolvation process is more evident on the (1–10) facet, as shown in Fig. 11. Optical images of QDMF crystals at different temperatures are shown in Fig. 11A, while Fig. 11B shows the corresponding Raman spectra. Surface changes are evident in the images, and the Raman spectra shows conversion of the QDMF into an anhydrous form previously observed upon dehydration of the stable quercetin dihydrate [35] (Fig. S8). Furthermore, Fig. 11C and Fig. 11D show SEM images of the (1–10) facet of an aged QDMF crystal: regular voids are present on this facet, possibly formed upon release of the DMF molecules characterizing this crystallographic plane.

In order to verify the differences in chemical nature of the three main QDMF facets, micro-Raman maps were acquired on cleaved and non-cleaved crystals of QDMF exposing the (1–10) and (001) facets. Fig. 12A shows the external surface (crystal freshly collected from the solvent) and the two facets after cleavage. No significant difference can be observed among the spectra, possibly due to the low sensitivity of the micro-Raman technique. However, differences can be observed after a few hours of exposure to the atmosphere. The changes are likely related to the desolvation process, also observed in Fig. 11, but it is evident that the mechanism and kinetics of desolvation are different for each facet, in agreement with the different surface chemistry calculated in Table 7. A further experiment was performed using 100× magnification: Raman mapping in x and y dimensions was conducted on the (1–10) non-cleaved facet and is reported in Fig. S9 and S10. Secondary nucleation fine particles were identified on this facet, but no significant differences in the spectra were detected, indicating uniformity across the facet.

The group of bands between 1500 and 1300 cm^{-1} can be linked to mechanical coupled vibrations of (C—C) stretching and in-plane (CH) and (C-OH) bending (36); specifically, the peaks within this interval are revealed at 1327, 1378, 1429 and 1502 cm^{-1}. The peak around 1568 cm^{-1} can be attributed to phenyl and benzo rings (C=C) stretching,

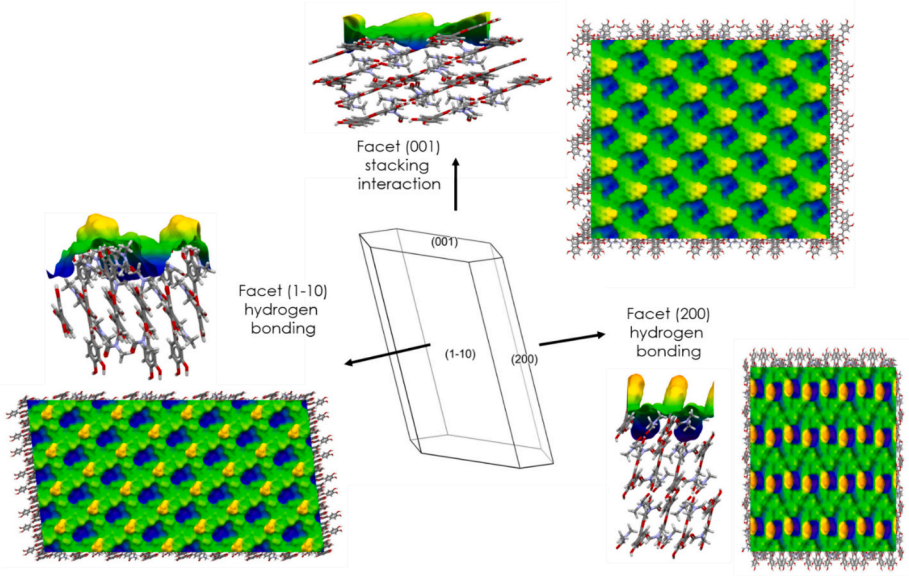

Fig. 9. Surface topology and rugosity comparison for QDMF: the average plane (green), region above the average plane (yellow), and region below the average plane (blue). The projected area of the three main facets (001), (1–10) and (200) are 61, 58, and 40 nm^2. The terminations of the facets are also shown. (For interpretation of the references to colour in this figure legend, the reader is referred to the web version of this article.)

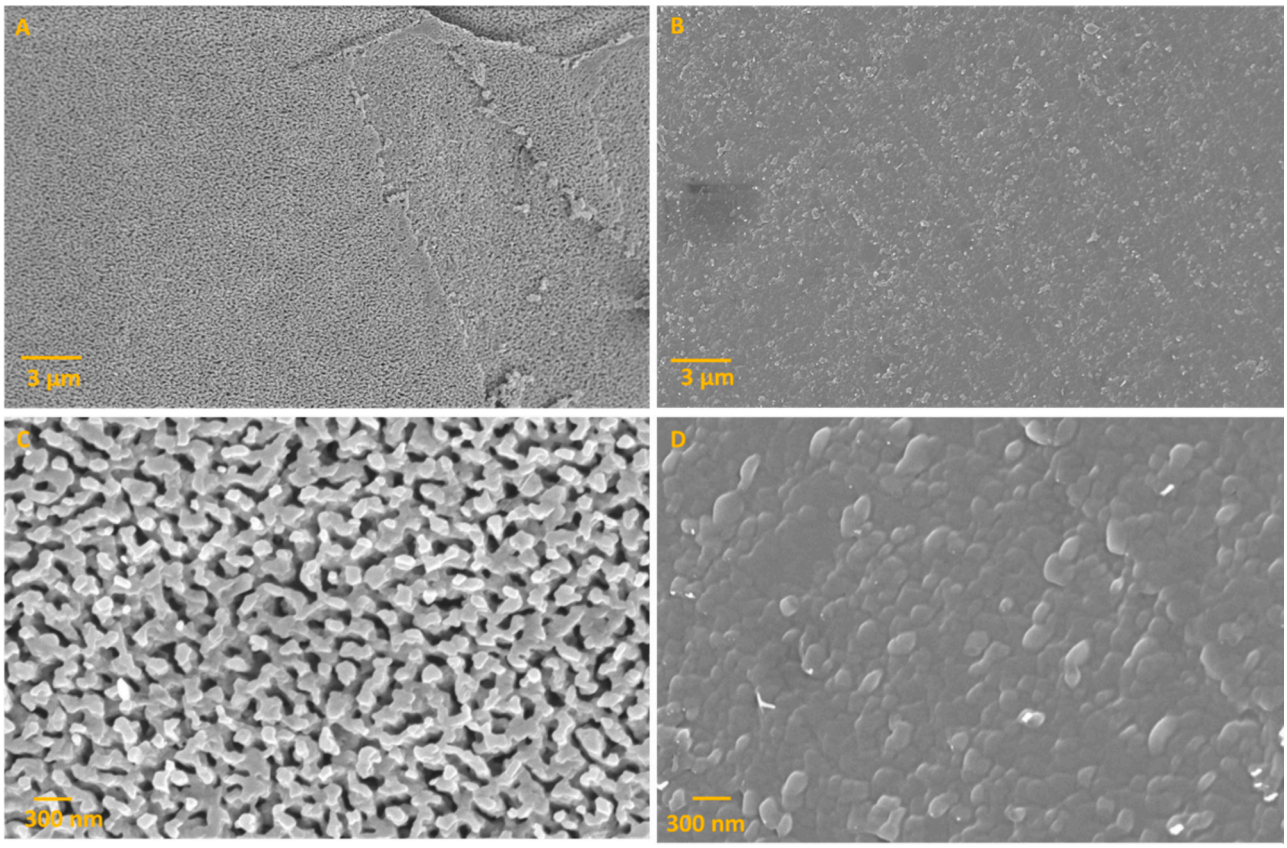

Fig. 10. SEM images of the {001} (A and C), and {110} (B and D) facets of cleaved crystal of QDMF at different magnifications.

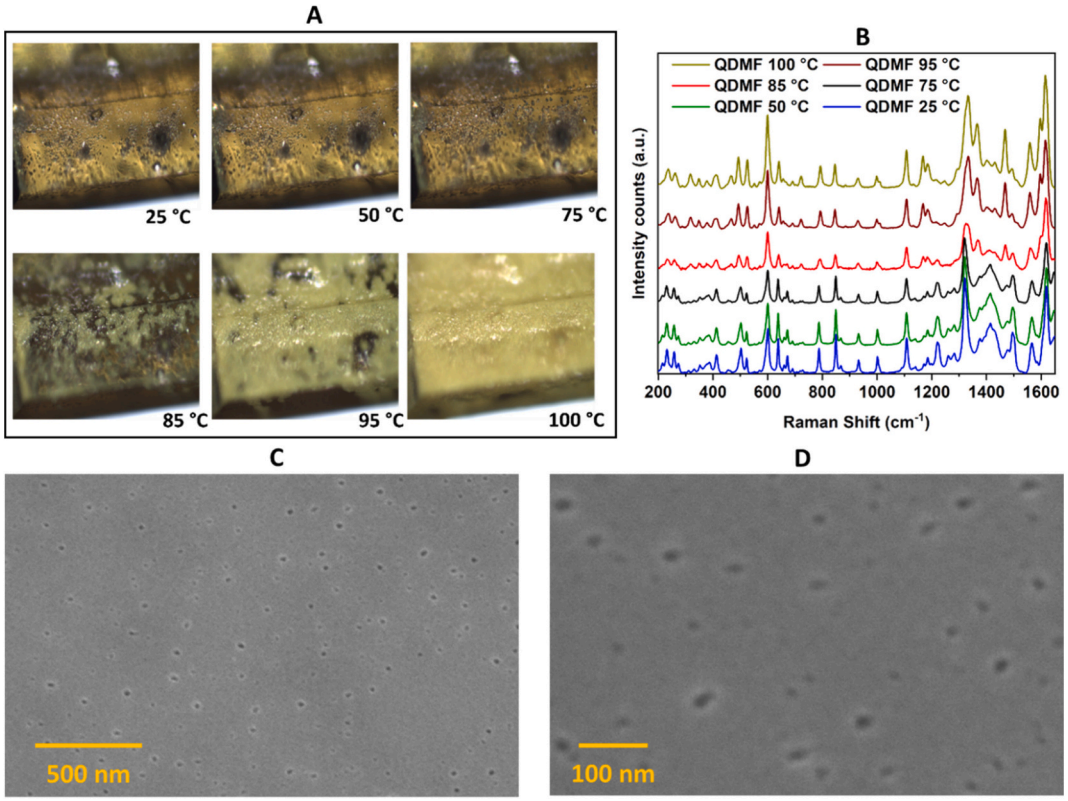

Fig. 11. QDMF desolvation process. (A) Optical images at different temperatures. (B) Raman spectra at different temperatures. (C) and (D) non cleaved (1–10) facet at two different SEM magnifications.

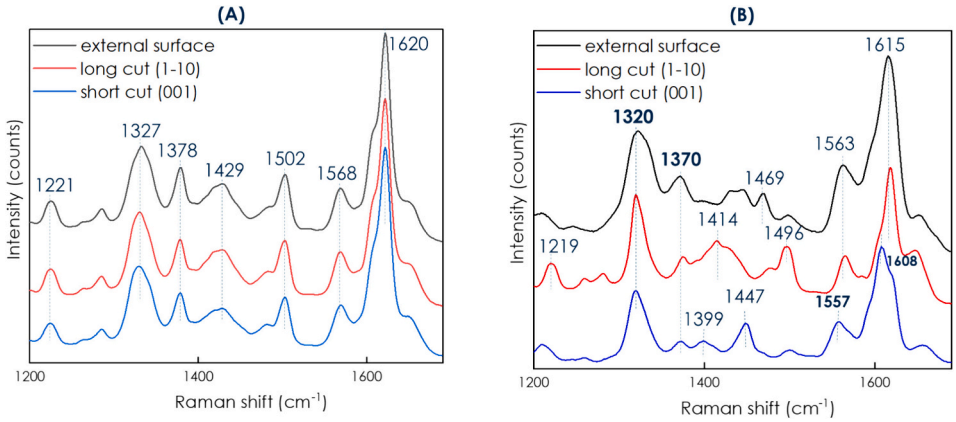

Fig. 12. Raman spectra for the (1–10) and (001) cleaved and the (1–10) uncleaved facet (external surface) immediately after sample preparation (A) and after several hours exposed to ambient conditions (B).

while the peaks at 1620 and 1654 cm^{-1} are associated with the (C=C) stretching and (C=O) stretching, respectively.

In conclusion, as schematically represented in Fig. 13, in this work combinations of different Particle Informatics tools such as synthon analysis, crystal structure visualization, and attachment energy calculations were used to model bulk and facet specific surface features of QDMF. Such simulated data were linked to important quality attributes of QDMF crystals; in particular, the desolvation behaviour, crystal anisotropy and facet specific properties (roughness and surface chemistry).

4. Conclusions

In this work Particle Informatics tools were used to model bulk and surface properties of a DMF solvate of quercetin, QDMF. The intrinsic synthon analysis showed prevalence of hydrogen bonds (around 40% of the total lattice energy) in the structure, together with off-set stacking of quercetin molecules (35.8% of the total lattice energy). From the attachment energy model, it was found that the largest {110} facet grows predominantly *via* hydrogen bonds, which explains the hydrophilic nature of this crystal structure, as shown by contact angle measurements. Additionally, it was found that DMF molecules in the QDMF structure are involved in two different quercetin-DMF synthons, which might explain why DMF desolvation happens in more than one step, with structural rearrangement in between (as demonstrated by DSC and TGA). The attachment energy model was also used to determine the chemical nature and topology of the three main facets identified experimentally, the (1–10), (200) and the (001). Significant differences in roughness and surface features between the rougher (200) facet and the other two were estimated. SEM images confirmed this surface anisotropy, although at a different scale compared to the modelling results.

Finally, it was found that the largest (1–10) facet is mostly occupied by exposed DMF molecules, which explains why desolvation preferentially happens on this facet; experimental evidence of this phenomenon was detected with SEM and Raman spectroscopy.

Our findings demonstrate that Particle Informatics tools are effective in predicting critical particle quality attributes, such as stability to desolvation, water wettability, and facet-specific anisotropy.

Formatting of funding sources

European Research Council (ERC) Starting Grant 949229 (CryForm).

CRediT authorship contribution statement

Emilia Prandini: Writing – original draft, Investigation, Formal analysis, Data curation. **Eleonora Calì:** Writing – review & editing,

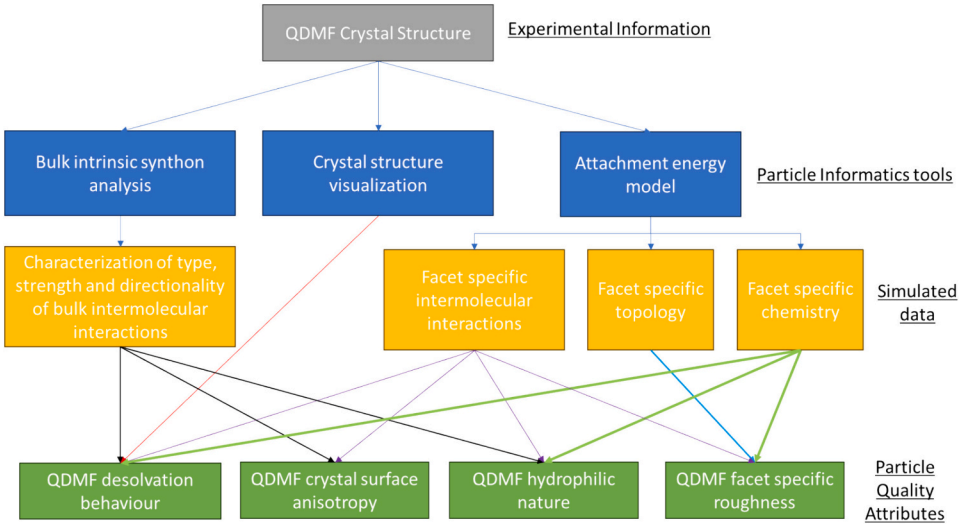

Fig. 13. Schematic representation of the Particle Informatics tools used in this paper, together with the resulting simulated data and related particle quality attributes.

Formal analysis, Data curation. **Andrew G.P. Maloney:** Writing – review & editing, Supervision, Funding acquisition, Formal analysis, Data curation. **Emmanuele Parisi:** Writing – review & editing, Writing – original draft, Investigation, Formal analysis, Data curation. **Elena Simone:** Writing – review & editing, Writing – original draft, Supervision, Resources, Funding acquisition, Data curation.

Declaration of competing interest

The authors declare that they have no known competing financial interests or personal relationships that could have appeared to influence the work reported in this paper.

Data availability

Data and metadata will be made open access in public repositories (CCDC, Zenodo, GitHub).

Acknowledgments

This project has received funding from the European Research Council (ERC) under the European Union's Horizon 2020 research and innovation program (grant agreement no. 949229, awarded to the corresponding author). The authors are grateful to the Cambridge Crystallographic Data Centre for co-funding the PhD scholarship. Many thanks to Alexandru A. Moldovan and Pietro Sacchi for providing the CSD Python API script and their helpful discussions.

Appendix A. Supplementary data

Supplementary data to this article can be found online at https://doi.org/10.1016/j.powtec.2024.119927.

References

[1] G.R. Desiraju, Crystal engineering: a holistic view, Angew. Chem. Int. Ed. 46 (2007) 8342–8356, https://doi.org/10.1002/anie.200700534.
[2] G.R. Desiraju, Crystal engineering: from molecule to crystal, J. Am. Chem. Soc. 135 (2013) 9952–9967, https://doi.org/10.1021/ja403264c.
[3] A.A. Moldovan, A.G.P. Maloney, Surface analysis—from crystal structures to particle properties, Cryst. Growth Des. 24 (10) (2024) 4160–4169, https://doi.org/10.1021/acs.cgd.4c00259.
[4] E. Simone, Z.K. Nagy, A link between the ATR-UV/Vis and Raman spectra of zwitterionic solutions and the polymorphic outcome in cooling crystallization, CrystEngComm 17 (2015) 6538–6547, https://doi.org/10.1039/c5ce00702j.
[5] E. Simone, A.N. Saleemi, N. Tonnon, Z.K. Nagy, Active polymorphic feedback control of crystallization processes using a combined raman and ATR-UV/Vis spectroscopy approach, Cryst. Growth Des. 14 (2014) 1839–1850.
[6] S. Agrawal, S.H. Rawal, V.R. Reddy, J.M. Merritt, Use of automation, dynamic image analysis, and process analytical technologies to enable data rich particle engineering efforts at the drug substance / drug product interface: a case study using lovastatin, Chem. Eng. Res. Des. 205 (2024) 578–590, https://doi.org/10.1016/j.cherd.2024.04.032.
[7] A. Reinhold, H. Briesen, High dimensional population balances for the growth of faceted crystals: combining Monte Carlo integral estimates and the method of characteristics, Chem. Eng. Sci. 127 (2015) 220–229, https://doi.org/10.1016/j.ces.2015.01.035.
[8] Y. Barhate, H. Kilari, W.-L. Wu, Z.K. Nagy, Population balance model enabled digital design and uncertainty analysis framework for continuous crystallization of pharmaceuticals using an automated platform with full recycle and minimal material use, Chem. Eng. Sci. 287 (2023) 119688, https://doi.org/10.1016/j.ces.2023.119688.
[9] A. Raponi, S. Romano, G. Battaglia, A. Buffo, M. Vanni, A. Cipollina, D. Marchisio, Computational modeling of magnesium hydroxide precipitation and kinetics parameters identification, Cryst. Growth Des. 23 (2023) 4748–4759, https://doi.org/10.1021/acs.cgd.2c01179.
[10] A. Raponi, R. Achermann, S. Romano, S. Trespi, M. Mazzotti, A. Cipollina, A. Buffo, M. Vanni, D. Marchisio, Population balance modelling of magnesium hydroxide precipitation: full validation on different reactor configurations, Chem. Eng. J. 477 (2023) 146540, https://doi.org/10.1016/j.cej.2023.146540.
[11] L. Metilli, L. Morris, A. Lazidis, S. Marty-Terrade, M. Holmes, M. Povey, E. Simone, Real-time monitoring of fat crystallization using pulsed acoustic spectroscopy and supervised machine learning, J. Food Eng. 335 (2022), https://doi.org/10.1016/j.jfoodeng.2022.111192.
[12] R. Docherty, K.J. Roberts, Modelling the morphology of molecular crystals; application to anthracene, biphenyl and β-succinic acid, J. Cryst. Growth 88 (1988) 159–168, https://doi.org/10.1016/0022-0248(88)90272-2.
[13] P. Klitou, I. Rosbottom, E. Simone, Synthonic modeling of quercetin and its hydrates: explaining crystallization behavior in terms of molecular conformation and crystal packing, Cryst. Growth Des. 19 (2019) 4774–4783, https://doi.org/10.1021/acs.cgd.9b00650.
[14] S.R. Alizadeh, M.A. Ebrahimzadeh, Quercetin derivatives: drug design, development, and biological activities, a review, Eur. J. Med. Chem. 229 (2022), https://doi.org/10.1016/j.ejmech.2021.114068.
[15] M. Rossi, L.F. Rickles, W.A. Halpin, The crystal and molecular structure of quercetin: a biologically active and naturally occurring flavonoid, Bioorg. Chem. 14 (1986) 55–69, https://doi.org/10.1016/0045-2068(86)90018-0.
[16] M.J. Bryant, A.G.P. Maloney, R.A. Sykes, Predicting mechanical properties of crystalline materials through topological analysis, CrystEngComm 20 (2018) 2698–2704, https://doi.org/10.1039/C8CE00454D.
[17] M.J. Bryant, I. Rosbottom, I.J. Bruno, R. Docherty, C.M. Edge, R.B. Hammond, R. Peeling, J. Pickering, K.J. Roberts, A.G.P. Maloney, "Particle informatics": advancing our understanding of particle properties through digital design, Cryst. Growth Des. 19 (2019) 5258–5266, https://doi.org/10.1021/acs.cgd.9b00654.
[18] P. Klitou, C.M. Pask, L. Onoufriadi, I. Rosbottom, E. Simone, Solid-state characterization and role of solvent molecules on the crystal structure, packing, and physiochemical properties of different quercetin solvates, Cryst. Growth Des. 20 (2020) 6573–6584, https://doi.org/10.1021/acs.cgd.0c00751.
[19] T.T.H. Nguyen, R.B. Hammond, I.D. Styliari, D. Murnane, K.J. Roberts, A digital workflow from crystallographic structure to single crystal particle attributes for predicting the formulation properties of terbutaline sulfate, CrystEngComm 22 (2020) 3347–3360, https://doi.org/10.1039/d0ce00026d.
[20] I. Rosbottom, T.D. Turner, C.Y. Ma, R.B. Hammond, K.J. Roberts, C.W. Yong, I. T. Todorov, The structural pathway from its solvated molecular state to the solution crystallisation of the α- and β-polymorphic forms of para amino benzoic acid, Faraday Discuss. 235 (2022) 467–489, https://doi.org/10.1039/d1fd00112d.
[21] T.T.H. Nguyen, I. Rosbottom, I. Marziano, R.B. Hammond, K.J. Roberts, Crystal morphology and interfacial stability of RS-ibuprofen in relation to its molecular and synthonic structure, Cryst. Growth Des. 17 (2017) 3088–3099, https://doi.org/10.1021/acs.cgd.6b01878.
[22] F.S. Gentile, E. Parisi, R. Centore, Virtual structures in polymorphic 5-nitrobenzo [c], CrystEngComm 25 (2023) 859–865, https://doi.org/10.1039/d2ce01619b.
[23] M.M. Haskins, N. Kavanagh, R. Sanii, S. Khorasani, J. Chen, Z. Zhang, X. Dai, B. Ren, T. Lu, M.J. Zaworotko, Tuning the Pharmacokinetic Performance of Quercetin by Cocrystallization, 2023, https://doi.org/10.1021/acs.cgd.3c00590.
[24] A.A. Moldovan, R.Y. Penchev, R.B. Hammond, J.P. Janowiak, T.E. Hardcastle, A.G. P. Maloney, S.D.A. Connell, Automated in silico energy mapping of facet-specific interparticle interactions, Cryst. Growth Des. 21 (2021) 5780–5791, https://doi.org/10.1021/acs.cgd.1c00674.
[25] C.Y. Ma, A.A. Moldovan, A.G.P. Maloney, K.J. Roberts, Exploring the CSD drug subset: an analysis of lattice energies and constituent intermolecular interactions for the crystal structures of pharmaceuticals, J. Pharm. Sci. 112 (2023) 435–445, https://doi.org/10.1016/j.xphs.2022.11.027.
[26] P. Klitou, I. Rosbottom, V. Karde, J.Y.Y. Heng, E. Simone, Relating crystal structure to surface properties: a study on quercetin solid forms, Cryst. Growth Des. 22 (2022) 6103–6113, https://doi.org/10.1021/acs.cgd.2c00707.
[27] I. Rosbottom, Examination of inequivalent wetting on the crystal habit surfaces of RS-ibuprofen using grid-based molecular modelling, Phys. Chem. Chem. Phys. 20 (2018) 11622–11633, https://doi.org/10.1039/C7CP08354H.
[28] I. Rosbottom, T.N.H. Cheng, J.Y.Y. Heng, Computational analysis of the solid-state and solvation properties of carbamazepine in relation to its polymorphism, Chem. Eng. Technol. 43 (2020) 1152–1159, https://doi.org/10.1002/ceat.202000056.
[29] M.J. Bryant, S.N. Black, H. Blade, R. Docherty, A.G.P. Maloney, S.C. Taylor, The CSD drug subset: the changing chemistry and crystallography of small molecule pharmaceuticals, J. Pharm. Sci. 108 (2019) 1655–1662, https://doi.org/10.1016/j.xphs.2018.12.011.
[30] D.E. Braun, S.R. Lingireddy, M.D. Beidelschies, R. Guo, P. Müller, S.L. Price, S. M. Reutzel-Edens, Unraveling complexity in the solid form screening of a pharmaceutical salt: why so many forms? Why so few? Cryst. Growth Des. 17 (2017) 5349–5365, https://doi.org/10.1021/acs.cgd.7b00842.
[31] I. Rosbottom, K.J. Roberts, R. Docherty, The solid state, surface and morphological properties of p-aminobenzoic acid in terms of the strength and directionality of its intermolecular synthons, CrystEngComm 17 (2015) 5768–5788, https://doi.org/10.1039/c5ce00302d.
[32] E. Hadjittofis, M.A. Isbell, V. Karde, S. Varghese, C. Ghoroi, J.Y.Y. Heng, Influences of crystal anisotropy in pharmaceutical process development, Pharm. Res. 35 (2018), https://doi.org/10.1007/s11095-018-2374-9.
[33] P.M. Shah, V. Vishnu Priya, R. Gayathri, Quercetin – a flavonoid:a systematic review, J. Pharm. Sci. Res. 8 (2016) 878–880.
[34] P. Duangiad, B. Nutho, T. Chaijarasphong, N.P. Morales, T. Pongtharangkul, I. Hamachi, A. Ojida, J. Wongkongkatep, Naturally occurring quercetin and myricetin as potent inhibitors for human ectonucleotide pyrophosphatase/phosphodiesterase 1, Sci. Rep. 14 (2024) 1–13, https://doi.org/10.1038/s41598-023-50590-7.
[35] P. Klitou, E. Parisi, S. Bordignon, F. Bravetti, I. Rosbottom, M. Dell'Aera, C. Cuocci, M.R. Chierotti, A. Altomare, E. Simone, Navigating the complex solid form landscape of the quercetin flavonoid molecule, Cryst. Growth Des. 23 (2023) 6034–6045, https://doi.org/10.1021/acs.cgd.3c00584.
[36] M. Ay, A. Charli, H. Jin, V. Anantharam, A. Kanthasamy, A.G. Kanthasamy, Chapter 32 - Quercetin, in: R.C. Gupta (Ed.), Nutraceuticals, Academic Press,

Boston, 2016, pp. 447–452, https://doi.org/10.1016/B978-0-12-802147-7.00032-2.
[37] K. Vasisht, K. Chadha, M. Karan, Y. Bhalla, A.K. Jena, R. Chadha, Enhancing biopharmaceutical parameters of bioflavonoid quercetin by cocrystallization, CrystEngComm 18 (2016) 1403–1415, https://doi.org/10.1039/C5CE01899D.
[38] M. Veverka, T. Dubaj, J. Gallovič, V. Jorík, E. Veverková, M. Danihelová, P. Šimon, Cocrystals of quercetin: synthesis, characterization, and screening of biological activity, Monatshefte Für Chem. Chem. Mon. 146 (2015) 99–109, https://doi.org/10.1007/s00706-014-1314-6.
[39] H. He, Y. Huang, Q. Zhang, J.-R. Wang, X. Mei, Zwitterionic Cocrystals of flavonoids and proline: solid-state characterization, pharmaceutical properties, and pharmacokinetic performance, Cryst. Growth Des. 16 (2016) 2348–2356, https://doi.org/10.1021/acs.cgd.6b00142.
[40] G.M. Sheldrick, SADABS, Empirical Absorption Correction Program; University of Göttingen: Göttingen, Germany, 1997, Google Scholar there Is no Corresponding Record for this Reference, 2002.
[41] R. Altomare, A. Burla, M.C. Camalli, M. Cascarano, G.L. Giacovazzo, C. Guagliardi, A. Moliterni, A.G.G. Polidori, G. Spagna, SIR97: a new tool for crystal structure determination and refinement, J. Appl. Crystallogr. 32 (1999) 115–119.
[42] G.M. Sheldrick, Crystal structure refinement with$\less$i$\greater${SHELXL}$ \less$/i$\greater$, Acta Crystallogr C Struct. Chem. 71 (2015) 3–8, https://doi.org/10.1107/s2053229614024218.
[43] L.J. Farrugia, WinGX and ORTEP for windows: an update, J. Appl. Crystallogr. 45 (2012) 849–854.
[44] P.A. Macrae, C.F. Bruno, I.J. Chisholm, J.A. Edgington, PaulR McCabe, P. Pidcock, E. Rodriguez-Monge, L. Taylor, R. de Streek, J. Van Wood, Mercury CSD 2.0 – new features for the visualization and investigation of crystal structures, J. Appl. Crystallogr. 41 (2008) 466–470.
[45] L. Caira, M.R. Bettinetti, G. Sorrenti, M. Catenacci, Relationships between structural and thermal properties of anhydrous and solvated crystalline forms of brodimoprim, J. Pharm. Sci. 96 (2007) 996–1007.
[46] N.L. Allan, A.L. Rohl, D.H. Gay, C.R.A. Catlow, R.J. Davey, W.C. Mackrodt, Calculated bulk and surface properties of sulfates, Faraday Discuss. 95 (1993) 273–280. https://api.semanticscholar.org/CorpusID:97908940.
[47] R. Montis, M.B. Hursthouse, J. Kendrick, J. Howe, R.J. Whitby, Combining structural rugosity and crystal packing comparison: a route to more polymorphs? Cryst. Growth Des. 22 (2022) 559–569, https://doi.org/10.1021/acs.cgd.1c01132.
[48] R. Montis, R.J. Davey, S.E. Wright, G.R. Woollam, A.J. Cruz-Cabeza, Transforming computed energy landscapes into experimental realities: the role of structural rugosity, Angew. Chem. Int. Ed. 59 (2020) 20357–20360, https://doi.org/10.1002/anie.202006939.
[49] V.L. Borghetti, G.S. Carini, J.P. Honorato, S.B. Ayala, A.P. Moreira, J.C.F. Bassani, Physicochemical properties and thermal stability of quercetin hydrates in the solid state, Thermochim. Acta 539 (2012) 109–114.
[50] P. Klitou, C.M. Pask, L. Onoufriadi, I. Rosbottom, E. Simone, Solid-state characterization and role of solvent molecules on the crystal structure, packing, and physiochemical properties of different quercetin solvates, Cryst. Growth Des. 20 (2020) 6573–6584, https://doi.org/10.1021/acs.cgd.0c00751.